Examination of Mars2020 shock-layer conditions via infrared laser absorption spectroscopy of CO 2 and CO

Christopher C Jelloian, Nicolas Q Minesi, R Mitchell Spearrin, Augustin Tibère-Inglesse, Megan E Macdonald, Brett A Cruden

Examination of Mars2020 shock-layer conditions via infrared laser absorption spectroscopy of CO_2 and CO

Christopher C. Jelloian*, Nicolas Q. Minesi †, and R. Mitchell Spearrin‡
University of California, Los Angeles (UCLA), Los Angeles, CA 90095, USA

Augustin Tibère-Inglesse§, Megan E. MacDonald¶, and Brett A. Cruden‖
NASA Ames Research Center, Moffett Field, CA 94035, USA

A mid-infrared laser absorption diagnostic was deployed to study a simulated Mars2020 shock layer in the Electric Arc Shock Tube (EAST) facility at NASA's Ames Research Center. Rapid RF-diplexing techniques enabled quantitative temperature and number density measurements of CO_2 and CO with µs-resolution over an incident shock velocity range of 1.39 – 3.75 km/s. Two interband cascade lasers were utilized at 4.17 and 4.19 µm to resolve eight CO_2 asymmetric stretch fundamental band (ν_3) transitions from two different vibrational levels: 00^00 (ground state) and 01^10 (first excited bending mode). The probed rotational levels span across J" = 58 to J" = 140. Results are compared to DPLR simulations of the shock layer using kinetic mechanisms of Johnston et al. and Cruden et al. At shock velocities below 3.1 km/s, the agreement between the measurements and the Johnston mechanism is typically within 5% for temperature and within 10% for number density. At shock velocities above 3.1 km/s, the CO_2 measurement becomes sensitive to a thin boundary layer and corrections of this effect are presented. On test cases with enough energy to dissociate CO_2, a quantum cascade laser scanned the P(2, 20), P(0, 31), and P(3, 14) transitions of the CO fundamental band at 4.98 µm. CO formation rate is measured to be close to the Johnston kinetic mechanism at low velocities, and then trending towards the Cruden kinetic mechanism at high velocities. On a few low velocity test cases, rovibrational relaxation of the Martian atmosphere is probed with µs resolution.

I. Nomenclature

A_{21}	=	Einstein A coefficient of spontaneous emission
B_{21}	=	Einstein B coefficient of stimulated emission
B_{12}	=	Einstein B coefficient of absorption
$E_{\text{rot},i}$	=	energy of rotational level i
$E_{\text{vib},i}$	=	energy of vibrational level i
c	=	speed of light
c_2	=	second radiation constant
h	=	Planck's constant
I_t	=	transmitted light intensity
I_0	=	incident light intensity
J''	=	lower state rotational quantum number
k	=	Boltzmann constant
L	=	pathlength
M	=	molecular weight
n	=	collisional broadening coefficient of temperature dependence
n_i	=	population of level i

*Ph.D. Candidate, Mechanical and Aerospace Engineering Department, Member AIAA.
†Postdoctoral Researcher, Mechanical and Aerospace Engineering Department, Member AIAA.
‡Associate Professor, Mechanical and Aerospace Engineering Department, Member AIAA.
§Postdoctoral Scholar, Aerothermodynamics Branch, Member AIAA
¶Senior Aerospace Engineer, Thermophysics Facilities Branch, Member AIAA
‖Senior Research Scientist, Aerothermodynamics Branch, AIAA Associate Fellow

P = pressure
Q = partition function
S_j = linestrength of transition j
T_{tr} = translational temperature
T_{rot} = rotational temperature
T_{vib} = vibrational temperature
U_{is} = incident shock wave velocity
v'' = lower state vibrational quantum number
X = mole fraction
α = absorbance
ν_0 = transition wavenumber center
$\Delta\nu_C$ = collisional (Lorentzian) FWHM
$\Delta\nu_D$ = Doppler (Gaussian) FWHM
δ_{99} = Boundary layer thickness
ϕ = lineshape function
γ_{A-B} = collisional broadening coefficient
$\mathcal{A}_i$ = absorbance area of transition i

II. Introduction

The Mars2020 mission successfully landed the Perseverance rover within the Jezero crater at the Octavia E. Butler landing site on February 18, 2021. The aeroshell of the Mars2020 mission was instrumented with the MEDLI2 sensor suite [1–3] to conduct measurements of the aerothermal environment upon entry, descent, and landing (EDL). Temperatures were recorded at multiple locations via thermocouples. Total heat flux was recorded on the backshell by two sensors (MEDTHERM, Model 22171-01KS) and the backshell radiative heating component was measured via a radiometer (MEDTHERM, Model 22160-22KS-1.410). Figure 1 shows the backshell instrumentation and compares the flight data to the NASA simulations [1]. The simulated radiative heat flux (shown in Fig. 1) is generally well captured by

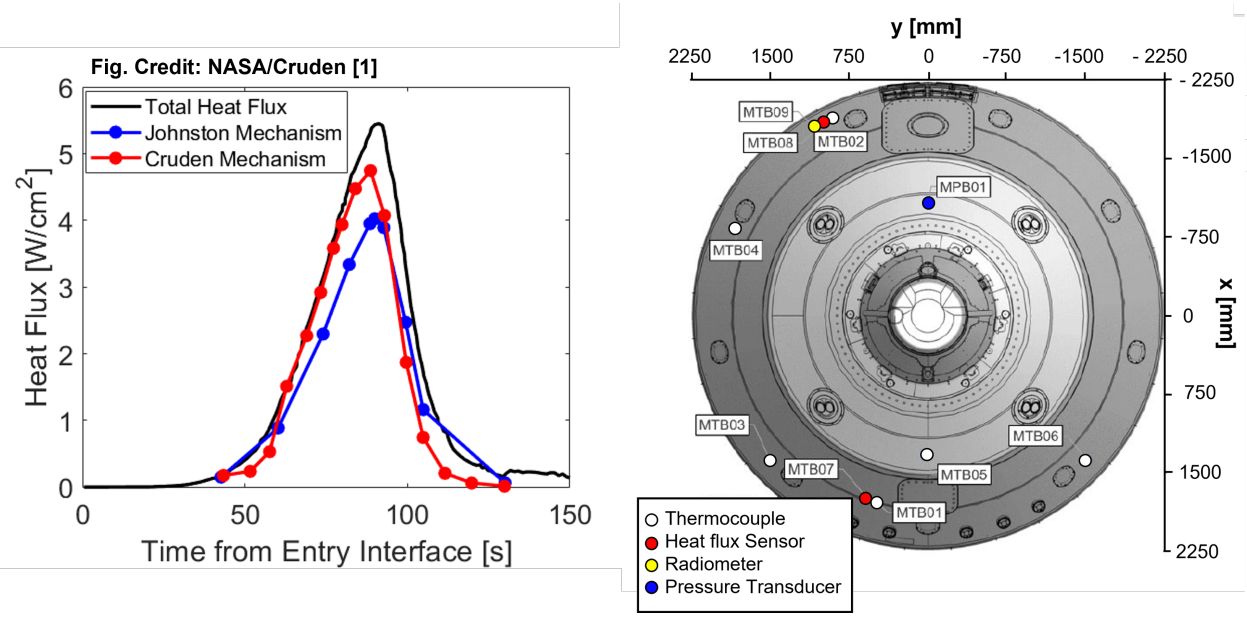

Fig. 1 (left) MEDLI2 flight data (total heat flux) compared to the radiative heat flux predicted by the Cruden [4] and Johnston [5] mechanisms at different points during entry. (right) Backshell measurement locations of the MEDLI2 sensor suite. Figure reproduced from [1–3, 6].

the NASA Cruden and Johnston models [4, 5], with under prediction at the peak. Some under prediction at the peak is expected, as the total heat flux is measured and the models have computed the radiative component. As the data shows,

convective heating is small at the MTB08/MTB09 position on the backshell. Interestingly, the Cruden mechanism matches the flight data well at early test times, and the Johnston mechanism performs better at later test times.

A test series (64A) at the Electric Arc Shock Tube (EAST) facility at NASA Ames was conducted to investigate the rate models at the Mars2020 conditions experienced by the MEDLI2 sensor in order to reduce uncertainties in the models. For that purpose, the EAST facility was equipped with several mid-infrared lasers for absorption spectroscopy measurements of temperature, CO, and CO_2 [7, 8]. In parallel, multiple spectrometers recorded plasma emission for additional measurements of temperature and number density. This work presents the laser absorption spectroscopy (LAS) results whereas a companion paper [9] details the optical emission spectroscopy (OES) results and compares the two techniques.

III. Methods and Theory

Laser absorption spectroscopy (LAS) is utilized to infer temperatures and number density of CO_2 and CO from spectrally-resolved light attenuation in the mid-wave infrared. LAS theory is well-detailed in literature [10], and key governing equations are briefly discussed in this section for context and nomenclature definition. The Beer-Lambert law, shown in Eq. 1, relates the spectral absorbance α at frequency ν to thermophysical gas properties (temperature, number density, velocity, etc.) via incident and transmitted light intensities, I_0 and I_t, respectively.

$$\alpha(\nu) = -\ln\left(\frac{I_t}{I_0}\right)_\nu = S_j(T_{\text{rot}}, T_{\text{vib}}) n_A L \phi_j(\nu, T_{\text{tr}}, P, X_A) \tag{1}$$

Here, n_A [molec·cm^{-3}] is the number density of the absorbing species A, L [cm] is the pathlength, $S_j(T_{\text{rot}}, T_{\text{vib}})$ [cm^{-1}/(molec·cm^{-2})] is the linestrength of rovibrational transition j at rotational temperature T_{rot} [K] and vibrational temperature T_{vib} [K], and $\phi_j(\nu, T_{\text{tr}}, P, X_A)$ [cm] is the lineshape function.

In this study, ϕ_j is resolved via scanned-wavelength laser absorption spectroscopy. There are two methods used to fit the measured absorbance spectrum: 1) A simulated spectrum can be fit over the entire range allowing temperature, number density, and line-specific collision width to float. 2) Each individual lineshape (ϕ_j) can be fit assuming a Voigt profile, without enforcing a single temperature or number density over all the features. Through analysis of the resulting absorbance area ratios, a temperature and number density can be determined. Method 2 can be advantageous if features are influenced by non-ideal effects such as a cool boundary layer, however there is a trade off when features become blended. Often this requires sequential fitting of the spectrum and this increases algorithmic complexity. The fitting routine employed in this work uses a step weight function, defined in Eq. 2. This weighting ensures that features of different amplitude equally contribute to the spectral fitting - see for instance the $\nu_3(00^00)$ R(58) and the $\nu_3(01^10)$ R(140) features in Fig. 2.

$$W_j = \frac{3}{\alpha_{max,j}} \tag{2}$$

The Voigt lineshape includes the Doppler and collisional broadening effects of the features as a convolution of Gaussian and Lorentzian profiles. The value of ϕ_j at the transition linecenter $\nu_{j,0}$ is expressed in Eq. 3, where a is the spectral damping parameter and $\Delta\nu_D$ [cm^{-1}] and $\Delta\nu_C$ [cm^{-1}] are the Doppler and collisional linewidth contributions, respectively.

$$\phi_j(\nu_{j,0}) = \frac{2}{\Delta\nu_D}\sqrt{\frac{\ln 2}{\pi}}\exp\left(a^2\right)[1 - \text{erf}(a)] \tag{3}$$

$$a = \frac{\sqrt{\ln 2}\Delta\nu_C}{\Delta\nu_D} \tag{4}$$

The Doppler linewidth depends on translational temperature T_{tr}, the molecular weight M [g·mol^{-1}] of the absorbing species, and the transition linecenter $\nu_{j,0}$ [cm^{-1}] as indicated in Eq. 5.

$$\Delta\nu_D = \nu_{J,0}(7.1623 \times 10^{-7})\sqrt{\frac{T_{\text{tr}}}{M}} \tag{5}$$

Collisional linewidth scales with pressure and the mole fraction weighted broadening coefficient of collision partner B with absorbing molecule A, as shown in Eq. 6. Additionally, the broadening coefficient (γ_{A-B}) is typically modeled by

implementing a power law, as shown in Eq. 7, where T_0 [K] is a reference temperature and n is the temperature exponent.

$$\Delta\nu_C = P \sum_B X_B 2\gamma_{A-B} \tag{6}$$

$$\gamma_{A-B}(T_{\mathrm{Tr}}) = \gamma_{A-B}(T_0)\left(\frac{T_0}{T_{\mathrm{Tr}}}\right)^n \tag{7}$$

$$\mathcal{A}_j = S_j(T_{\mathrm{rot}}, T_{\mathrm{vib}}) n_A L \tag{8}$$

Absorbance area is a function of the temperature dependent linestrength, number density and pathlength of the measurement (Eq. 8). Temperature is sensitive to the absorbance area ratios as shown in Eq. 9, relating absorbance areas to the relative linestrengths and associated state populations. The linestrength, S_j, is defined in Eq. 10, accounting for stimulated emission.

$$\frac{\mathcal{A}_1}{\mathcal{A}_2} = \frac{S_1(T_{\mathrm{rot}}, T_{\mathrm{vib}})}{S_2(T_{\mathrm{rot}}, T_{\mathrm{vib}})} \tag{9}$$

$$S_j = (n_1 B_{12} - n_2 B_{21})\frac{h\nu}{c} \tag{10}$$

B_{12} and B_{21} are the Einstein coefficients for absorption and stimulated emission, which are calculated from the Einstein A coefficient (A_{21}) tabulated in HITEMP [11], h is Planck's constant, ν is the wavenumber of the transition, c is the speed of light, n_1 and n_2 are the populations of the lower and upper levels respectively. By assuming separable Boltzmann populations over rotation and vibration, Eq. 10 can be rewritten as Eq. 11, where g_2 is the upper level degeneracy of the transition, $E_{\mathrm{rot},1}$ and $E_{\mathrm{vib},1}$ are the rotational and vibrational energies of the lower state, $E_{\mathrm{rot},2}$ and $E_{\mathrm{vib},2}$ are the rotational and vibrational energies of the upper state, Q_{rot} and Q_{vib} are the partition functions of rotation and vibration taken from NEQAIR [12].

$$S_j = \frac{A_{21} g_2}{8\pi\nu^2 c Q_{\mathrm{rot}}(T_{\mathrm{rot}}) Q_{\mathrm{vib}}(T_{\mathrm{vib}})}\left[\exp\left(\frac{-c_2 E_{\mathrm{rot},1}}{T_{\mathrm{rot}}}\right)\exp\left(\frac{-c_2 E_{\mathrm{vib},1}}{T_{\mathrm{vib}}}\right) - \exp\left(\frac{-c_2 E_{\mathrm{rot},2}}{T_{\mathrm{rot}}}\right)\exp\left(\frac{-c_2 E_{\mathrm{vib},2}}{T_{\mathrm{vib}}}\right)\right] \tag{11}$$

It is important to note that CO_2 has three vibrational modes; symmetric stretch (ss), doubly degenerate bending (bend), and asymmetric stretch (as) that may be at separate temperatures. In the case where $T_{ss} \neq T_{bend} \neq T_{as}$, Eq. 11, the vibrational energy terms and vibrational partition function in Eq. 11 must be both split into three terms representing each mode.

A. Line selection

In this work, a total of twelve spectral transitions (see Table 1) are targeted near 4.17, 4.19, and 4.98 µm to resolve temperatures and number densities of both CO_2 and CO. These lines were selected for strong absorbance signals over a wide range of temperatures with sufficient spectral isolation to enable resolution of individual integrated areas, and large energy level spacing making the measurement sensitive to temperature.

The carbon dioxide molecule possesses multiple modes of vibration, complicating the spectrum. The fundamental vibrational frequencies of CO_2 are: symmetric stretch (ν_1, 1334 cm^{-1}), doubly degenerate bending (ν_2, 667 cm^{-1}), and asymmetric stretch (ν_3, 2349 cm^{-1}). In this study, the CO_2 spectra are from the strong absorption region near 4.3 µm which corresponds to the fundamental asymmetric stretch bands (ν_3) where $\Delta v_3 = 1$. The fundamental asymmetric stretch bands can be distinguished by their lower vibrational levels, denoted with vibrational quantum numbers $v_1 v_2^{l_2} v_3$. l_2 characterizes the angular momentum of the molecule. Within the vibrational bands, rotational lines are indicated as X(J") where X is the branch (R, P, or Q) describing an increase, decrease, or no change in rotational quantum number, with J" being the lower state rotational assignment. In this work, we probe two ν_3 fundamental bands, notated as $\nu_3(00^00)$ and $\nu_3(01^10)$, and several rotational lines within the R branch of these bands ranging from J" = 58 to J" = 140. The target absorption transitions of CO_2 are shown in Fig. 2. The two bands utilized in this study are distinguished by lower vibrational energy level of the bending mode, (differentiated by colors in Fig. 2: black for the ground state, 00^00, and red for the first excited bending mode, 01^10) as both bands originate from the ground vibrational state of the symmetric ($v_1 = 0$) and asymmetric ($v_3 = 0$) stretch. The $\nu_3(00^00)$ R(58) line and the $\nu_3(01^10)$ R(103), R(104), and R(140) transitions are targeted for measurement by an interband cascade laser (ICL) at 4.19 µm. A second ICL is used at 4.17 µm to probe the $\nu_3(00^00)$ R(110), R(112), R(132), and R(134) features. This multi-laser sensing strategy

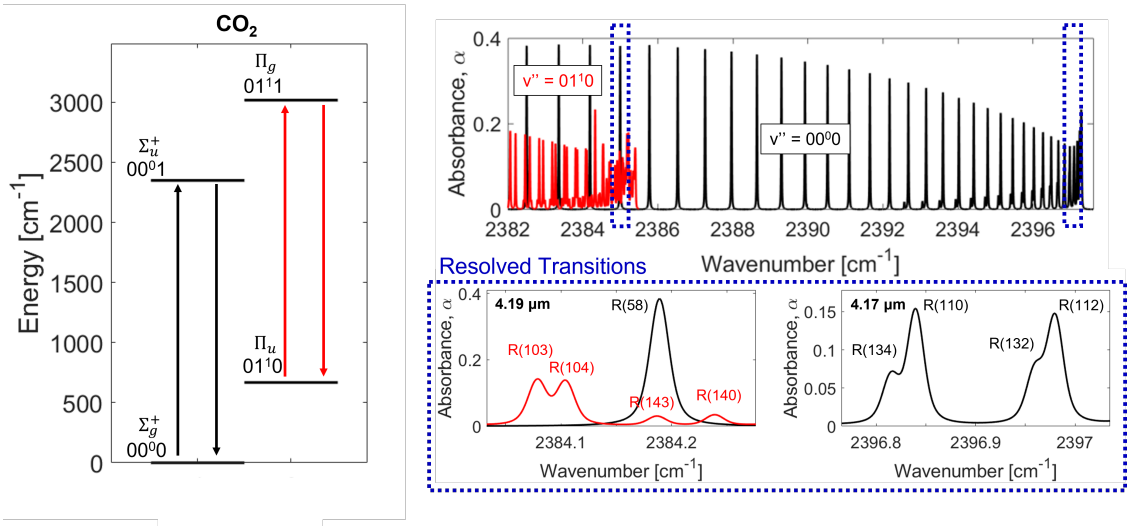

Fig. 2 (left) Energy level diagram of CO_2 showing the vibrational levels of interest in this study (rotational energy levels not shown). Note the CO_2 multiplicity (Σ, Π, etc.) varies with the bending excitation. (right) Simulated spectra at 3000 K (95% CO_2, 0.25 atm, L = 10.16 cm) using the HITEMP database [11]. Vibrational lower state is denoted with the color, and the transitions probed by the interband cascade lasers (ICL) are highlighted in the boxed regions.

improves the confidence in the temperature and CO_2 number density measurement. The CO_2 temperature sensitivity is mainly driven by the line pair of $\nu_3(00^00)$ R(58) and the $\nu_3(01^10)$ R(140) features whose maximum energy difference is $\Delta E'' = 7004$ cm^{-1}. At some low temperature conditions the $\nu_3(00^00)$ R(58) is optically thick, when this occurs the temperature sensitivity is mainly driven by the $\nu_3(01^10)$ R(103) and $\nu_3(01^10)$ R(140) line pair with $\Delta E'' = 3502$ cm^{-1}.

Table 1 Rotational and vibrational lower state energies of transitions probed in this work. $E''_{total} = E''_{vib} + E''_{rot}$. Linecenter and energies are given in wavenumber [cm^{-1}].

Molecule	Linecenter	Line Label	E''_{vib}	E''_{rot}	E''_{total}
CO	2008.42	P(2, 20)	4260	792	5052
CO	2008.53	P(0, 31)	0	1901	1901
CO	2008.55	P(3, 14)	6350	392	6742
CO_2	2384.08	$\nu_3(01^10)$ R(103)	667	4169	4836
CO_2	2384.10	$\nu_3(01^10)$ R(104)	667	4257	4924
CO_2	2384.19	$\nu_3(01^10)$ R(143)	667	7987	8654
CO_2	2384.19	$\nu_3(00^00)$ R(58)	0	1334	1334
CO_2	2384.24	$\nu_3(01^10)$ R(140)	667	7671	8338
CO_2	2396.81	$\nu_3(00^00)$ R(134)	0	7015	7015
CO_2	2396.84	$\nu_3(00^00)$ R(110)	0	4745	4745
CO_2	2396.96	$\nu_3(00^00)$ R(132)	0	6810	6810
CO_2	2396.98	$\nu_3(00^00)$ R(112)	0	4917	4917

For CO, the line identifier B(v'',J'') indicates the branch (R or P) and lower state vibrational and rotational quantum numbers. As shown in Fig. 3, the P(2, 20), P(0, 31), and P(3, 14) lines are targeted for measurement. This line selection has been used in previous work and demonstrated high sensitivity to number density and temperature [7].

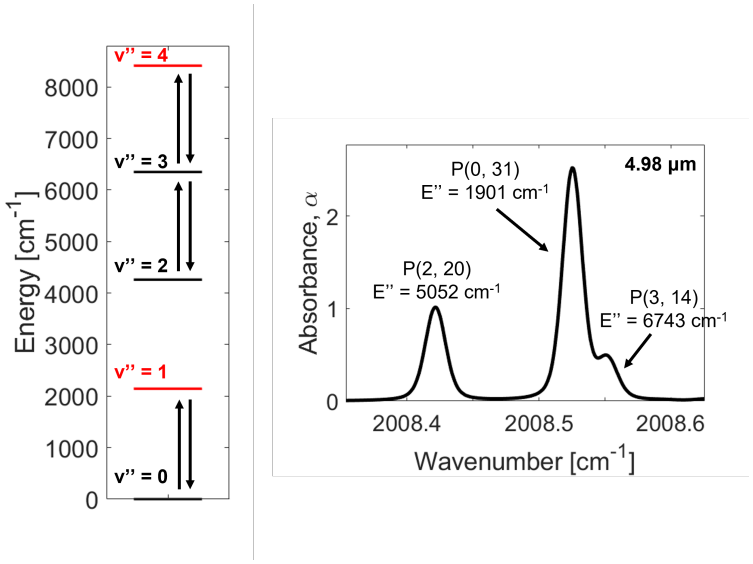

Fig. 3 (left) Energy level diagram of CO molecule showing vibrational levels of interest in this study. Red levels are not probed but will contribute to the intensity of the spectral features through stimulated emission. (right) CO spectrum simulated at 3000 K, 20% CO, 0.25 atm, and 10.16 cm pathlength using the HITEMP database [11].

.

B. Experimental Setup and Test Conditions

To resolve the spectral features described above in Sec. III.A, two beam paths are utilized with three lasers as shown in Fig. 4. Two NanoPlus interband cascade lasers (ICLs) were utilized near 4.19 and 4.17 µm to measure CO_2 and one Alpes quantum cascade laser was utilized near 4.98 µm to measure CO. The light is focused into InF_3 single mode fibers and mounted directly to EAST. The light is collimated upon exiting the fiber and pitched across the shock tube's 4-inch pathlength (= 10.16 cm). High bandwidth (~200 MHz) photovoltaic Vigo detectors are mounted approximately 4 inches from the optical port and contain an iris, bandpass filter, and focusing lens to cut emission, maximize signal, and minimize beam steering. For shock velocities above ~ 2.7 km/s, the temperature is high enough to dissociate CO_2 and form CO in sufficient quantities to be detected. In these cases, the 4.17-µm ICL laser used for CO_2 is replaced by a quantum cascade laser (QCL) scanning at 2008 cm^{-1} (= 4.98 µm) to monitor CO formation.

The EAST facility at NASA Ames was used to generate the conditions of interest for this study. This facility is well documented in literature [13] and is briefly described below. A 1.25 MJ capacitor bank supplies energy for the electric arc driver. The facility is capable of generating incident shock velocities up to 46 km/s through the 30-foot driven section though in this study the shock velocities ranged from 1.30 - 3.75 km/s. Approximately 50 shocks were conducted using a simulated Mars atmosphere at the time of the Mars2020 entry (95.4% CO_2, 2.6% N_2, 2.0% Ar) [14]. Different fill pressures were used ranging from 0.5 - 2.0 Torr on most test cases.

IV. Results

Experiments were conducted to reproduce the Mars2020 shock layer environment near the radiometer and nearby thermal plug location on the TPS. To achieve similarity, three primary fill pressures were used (1.09, 1.49, and 1.99 Torr) and various shock velocities ranging from 1.30 - 3.75 km/s captured multiple points along the flight trajectory. As a result, both chemically frozen and chemically reacting cases were observed. For all but the lowest velocities, vibrational relaxation times predicted by Park [15] and Simpson et al. [16] are on the order of 1 µs. Therefore, given the temporal resolution of the measurement, a 1 temperature spectrum is valid over almost the entire test time.

A. Spectrum Fitting Method Results

Absorbance is related to the temperature and number density as described in Sec. III. A single temperature spectrum is fit over the absorbance signals of each molecule independently allowing the temperature, number density and

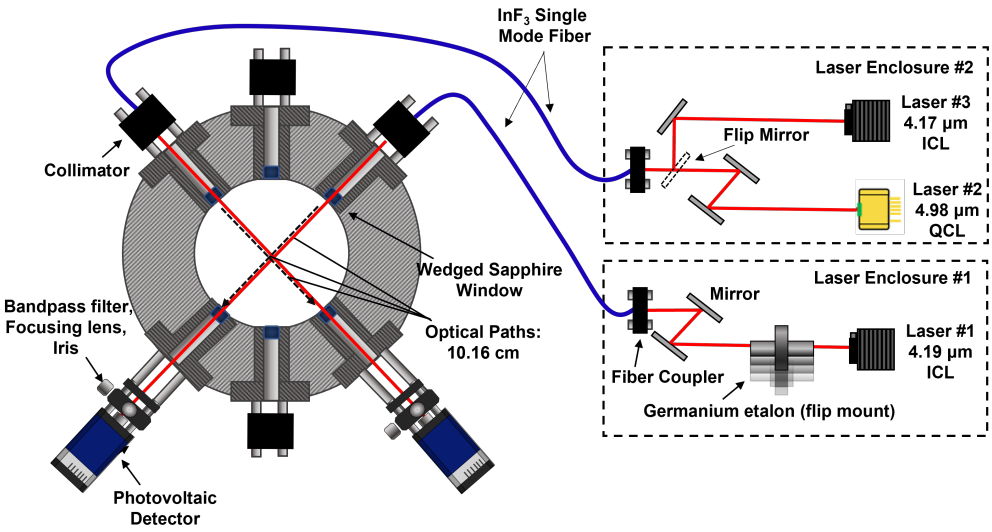

Fig. 4 Optical setup on the EAST facility. Two laser enclosures contain the free space beam and couple the light into InF_3 single mode fibers. The 4.17-µm ICL laser or the 4.98-µm QCL laser were used depending on the expected shock speed.

collisional broadening to float. Representative Voigt fits are shown in Figs. 5 and 6. The states that are probed in this

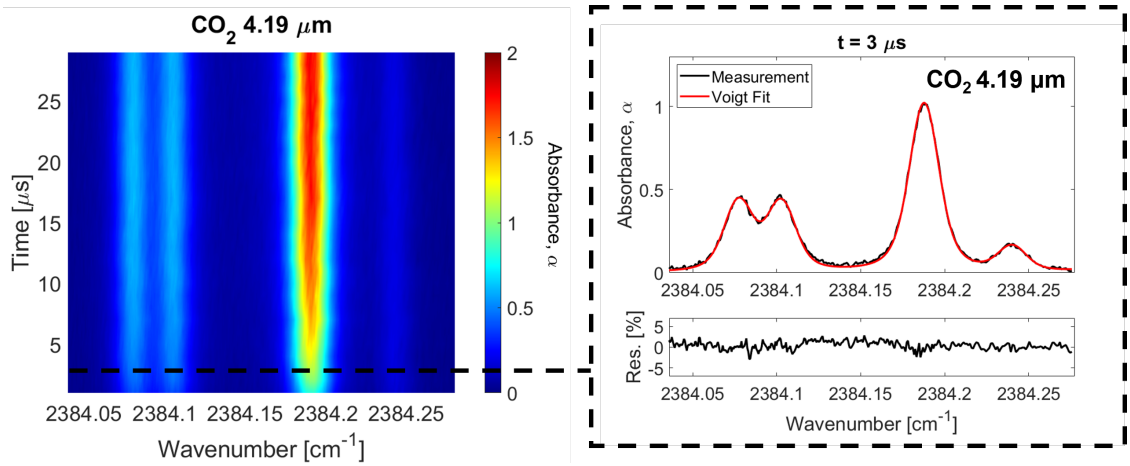

Fig. 5 (left) Absorbance vs wavenumber and time for CO_2 spectrum at 4.98 µm. (right) Representative Voigt fit of spectrum at t = 3 µs.

study become populated very rapidly behind the shock front and this results in high SNR at both wavelengths. The features are well resolved and the Voigt fit shows a low residual indicating it is a good model of the lineshape. Both signals are increasing throughout the test times due to two effects. 1) The CO signal increases primarily as more CO is formed. 2) As the gas cools due to dissociation, the CO_2 signal increases as the low lying states that are resolved in this work become more populated. The transients seen in the absorbance signal imply changing temperature and number density conditions throughout the test.

Key comparisons are made in Figs. 7 - 9 between the time resolved species and number densities resolved with LAS and the NASA DPLR CFD code [17]. From shock velocities below 2.7 km/s, CO_2 dissociation is frozen, and thus the simulation is independent of chemical kinetic mechanism used. As velocities increase above 2.7 km/s, dissociation begins to occur within the test time of the incident shock and the CFD simulation becomes sensitive to the chemical rate models employed.

The time resolved measurements generated with the single temperature spectrum fitting method show strong

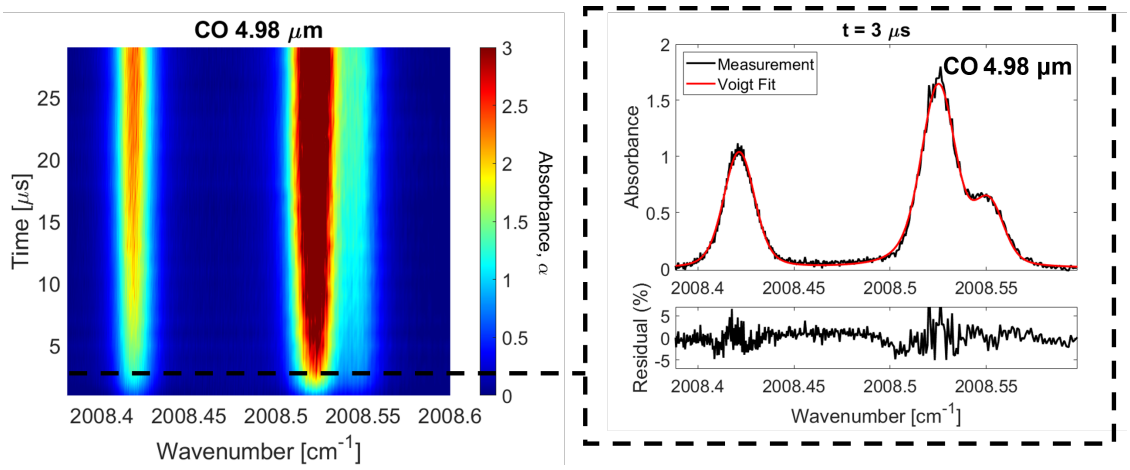

Fig. 6 (left) Absorbance vs wavenumber and time for CO spectrum at 4.98 µm. (right) Representative Voigt fit of spectrum at t = 3 µs.

agreement with the simulated temperature and number density across all chemically frozen test cases (see Figs. 7 - 8). On the time resolved temperature and species plots, number density and temperature in the first 1 - 2 microseconds may be elevated compared to the values measured at t > 2 μs and this is attributed to vibrational relaxation. When this was observed, the measurement resolution (1 µs) is faster than the vibrational relaxation time. In these cases, an alternative fitting routine based on the area ratio of two absorption features sensitive to rotational temperature was utilized to determine T_{rot}. The vibrational temperature is simultaneously deduced based on conservation of enthalpy (assuming $T_{rot} \neq T_{ss} = T_{bend} = T_{as}$). Lastly, the 1.99 Torr test cases produced a more optically thick spectrum than other fill pressures. Neglecting absorbance $\alpha > 3.0$ in the fit, the temperature measurement showed good agreement with the simulated temperature, however the number density of CO_2 is about 5 - 10% below that predicted. This discrepancy is attributed to the optical thickness. In Section IV.C, a rotational temperature fitting method neglecting the optically thick $\nu_3(00^00)$ R(58) feature is applied to the 1.99-Torr fill cases and reduces the gap between the simulations and measurements in number density.

Figures 7 - 8 are typical of the majority of 1.09 Torr and 1.49 Torr fill pressure test cases with velocities below ~2.7 km/s. Strong agreement is seen between the measured temperature and measured number density and the simulation. Figure 9 shows the typical inferred LAS temperature and number density trends of the higher velocity (>2.7 km/s) test cases. Independently measured temperature between CO_2 and CO is found to be in agreement and follow the DPLR Johnston [5] model. Additionally, the measured number density of CO_2 slightly decreases over the test time and is seen to be below the number densities predicted from both the Cruden [18] and Johnston models [5]. This difference can be attributed to the formation of a boundary layer and detailed analysis is presented in Sec. IV.B.

The CO number density results are highlighted in Fig. 10, and resolve a clear trend with lower shock velocities producing less CO. The yield of CO is determined via fitting an exponential curve (Eq. 12) to the CO number density and is compared to the Johnston [5] and Cruden [4] kinetic models implemented in DPLR.

$$n(t) = n_{eq}[1 - \exp\left(\frac{-t}{\tau}\right)] \tag{12}$$

The CO measurements are found to be in close agreement with the DPLR prediction, lying mostly along the Johnston [5] model and then in between the Cruden [4] and Johnston [5] models at higher velocities.

Figure 11 compares the average temperature predicted from the DPLR simulation based on the Johnston model [5] to the average temperature measured for the range of shock velocities covered in this test series. On a majority of the test cases, temperature is within 5% of the model. Number density measurements are typically within 10% of the model at velocities below 2.7 km/s, and then are systematically lower by 10 - 20%. This is attributed to the boundary layer (see Sec. IV.B). Additionally, two tests were performed at fill pressures of 9 Torr, to investigate CO formation at low velocity, but none was observed at 4.98 µm. CO_2 at 4.19 µm on these tests was optically thick precluding a measurement with this sensor at this condition.

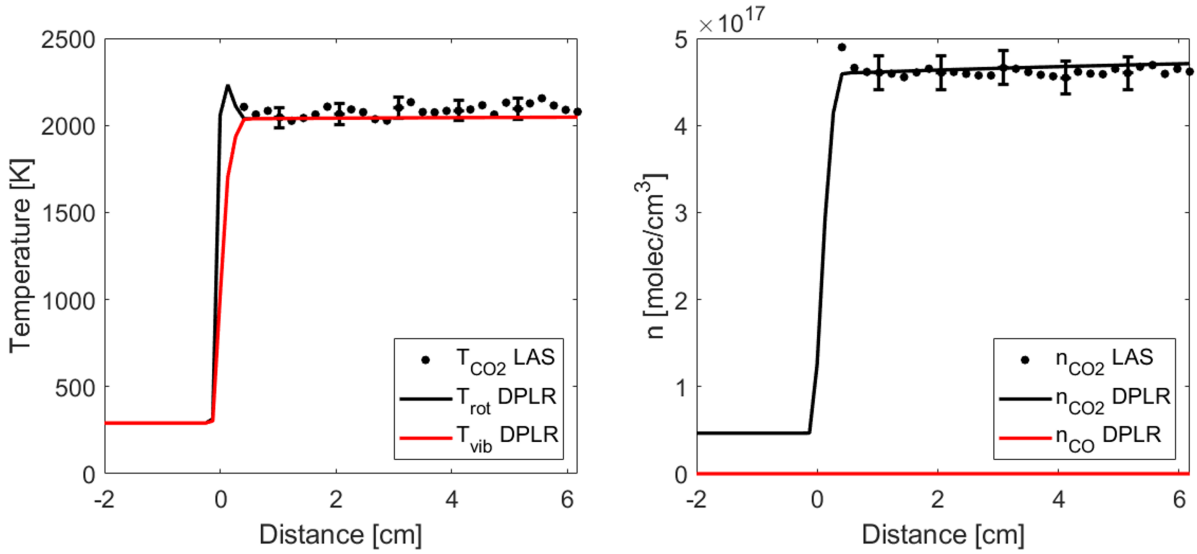

Fig. 7 Temperature (left) and number density (right) measured and simulated vs distance for a shock velocity of 2.06 km/s 1.49 Torr fill pressure. Estimated δT ~ 2.8 %, and δn ~ 6.0%.

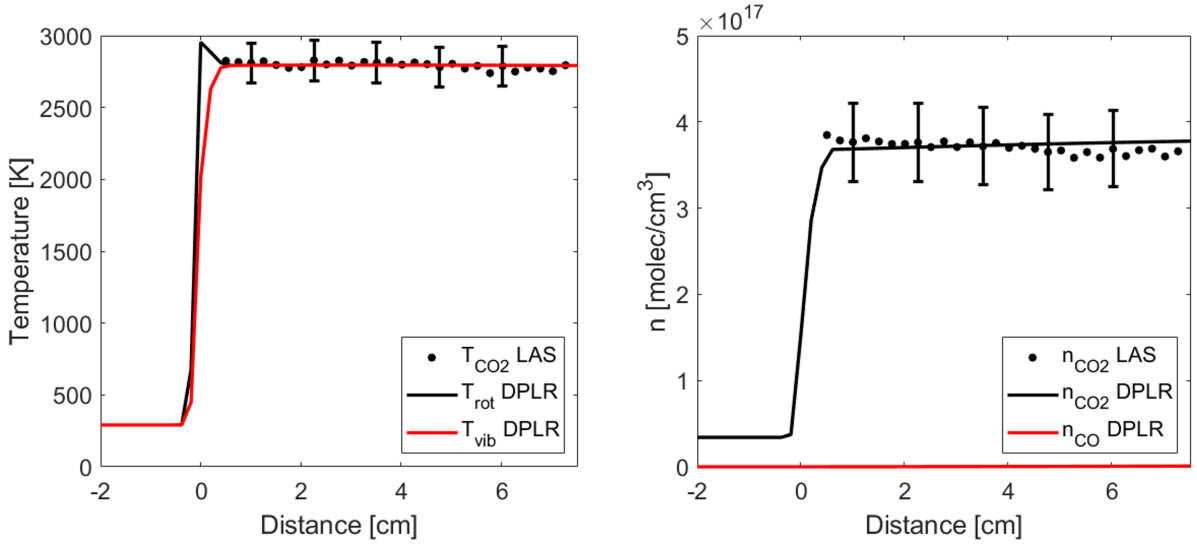

Fig. 8 Temperature (left) and number density (right) measured and simulated vs distance for a shock velocity of 2.51 km/s, 1.09 Torr fill pressure. Estimated δT ~ 5.0 %, and δn ~ 12.0%.

B. Boundary Layer Analysis

The discrepancy observed at high velocities between the number density of CO_2 inferred from absorption and the simulated number density was investigated and can be attributed to a thin boundary layer behind the shock wave. The following analysis is conducted to estimate the boundary layer and show its effect on inferred temperature and number density over a range of conditions. The compressible boundary layer in a shock tube is well described by Mirels theory [19] and the governing equations are shown in Eqs. 13 - 16.

$$\frac{\partial(\rho u)}{\partial x} + \frac{\partial(\rho v)}{\partial y} = 0 \qquad \text{(Mass)} \tag{13}$$

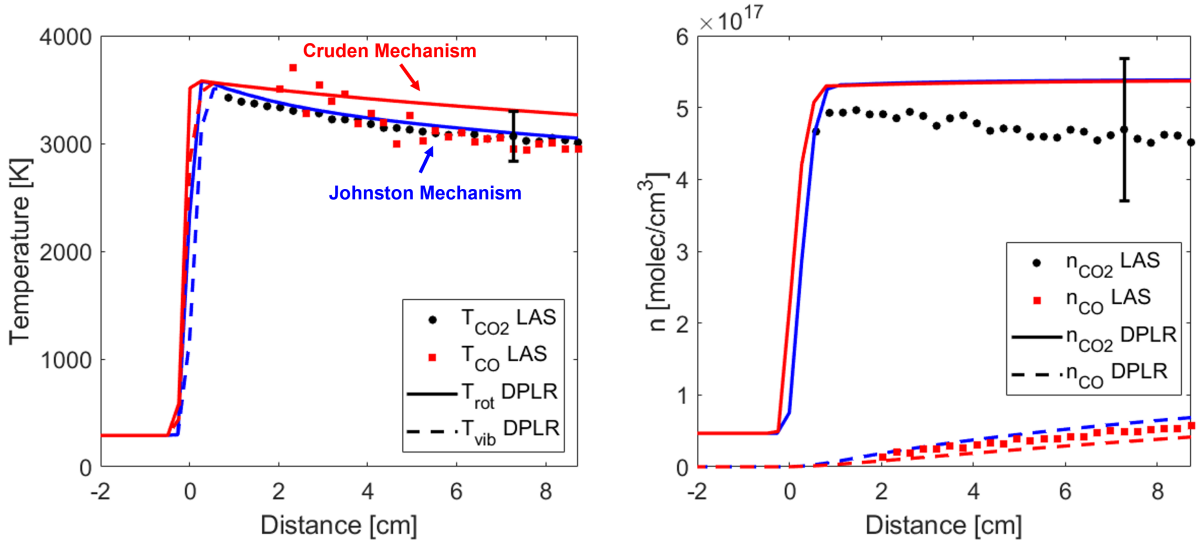

Fig. 9 Temperature (left) and number density (right) measured and simulated vs distance for a shock velocity of 2.91 km/s, 1.49 Torr fill pressure. Estimated δT ~ 7.5 %, and δn ~ 21.1%. Results have not been corrected for boundary layer absorption.

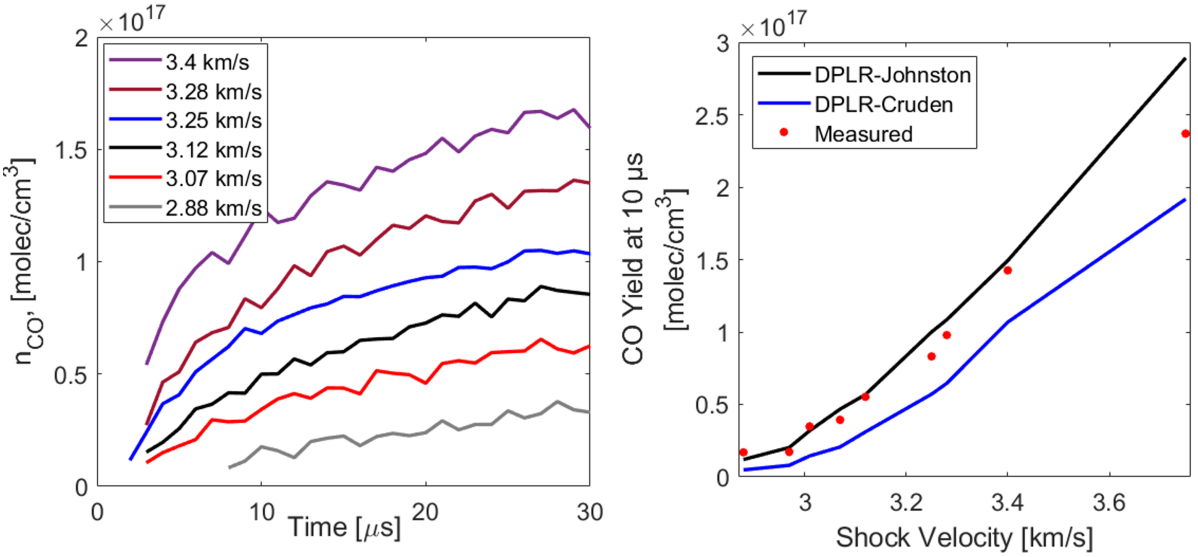

Fig. 10 (left) Measured CO number density with time for 1 Torr test cases. (right) CO yield at 10 µs from measurement and simulations vs shock velocity.

$$\rho\left(u\frac{\partial u}{\partial x}+v\frac{\partial u}{\partial y}\right)=-\frac{\partial p}{\partial x}+\frac{\partial}{\partial y}\left(\mu\frac{\partial u}{\partial y}\right) \qquad \text{(x - momentum)} \tag{14}$$

$$\frac{\partial p}{\partial y}=0 \qquad \text{(y - momentum)} \tag{15}$$

$$\rho c_p\left(u\frac{\partial T}{\partial x}+v\frac{\partial T}{\partial y}\right)=-u\frac{\partial p}{\partial x}+\frac{\partial}{\partial y}\left(k\frac{\partial T}{\partial y}\right)+\mu\left(\frac{\partial u}{\partial y}\right)^2 \qquad \text{(Energy)} \tag{16}$$

ρ is the density, u and v are the velocity in the flow (x) and wall normal (y) directions, p is the pressure, T is the temperature, μ is the dynamic viscosity, c_p is the specific heat at constant pressure, and k is the thermal conductivity of the gas. Dynamic viscosity and thermal conductivity are calculated at elevated temperatures via Sutherland's law [20]

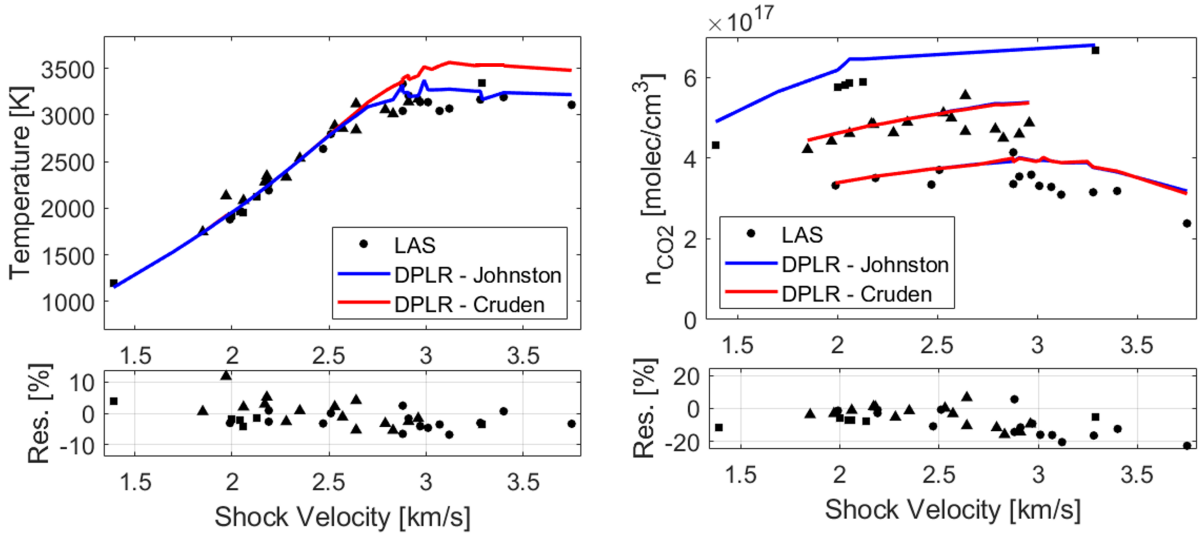

Fig. 11 CO_2 shock summary showing the average measured temperature and number density with the simulation, vs shock velocity. Residual is calculated against the Johnston mechanism [5]. Squares, triangles, and circles denote a fill pressure of 1.99, 1.49, and 1.09 Torr respectively.

as shown in Eqs. 17 and 18.

$$\frac{\mu}{\mu_0} = \left(\frac{T}{T_0}\right)^{\frac{3}{2}} \frac{T_0 + S_\mu}{T + S_\mu} \tag{17}$$

$$\frac{k}{k_0} = \left(\frac{T}{T_0}\right)^{\frac{3}{2}} \frac{T_0 + S_k}{T + S_k} \tag{18}$$

Sutherland's law is based on kinetic theory, and has been shown to be accurate over a wide range of temperatures for air and is commonly used in hypersonics CFD programs. For the simulation of the compressible boundary layer in this study, the gas viscosity is assumed to be that of CO_2, as it is the major constituent (95.4%) of the mixture. Table 1-2 and 1-3 of [20] list the viscosity of CO_2 as 1.370×10^{-5} [(N·s)/m^2] and thermal conductivity of CO_2 as 0.0146 [W/(m·K)] at the reference temperature of 273 K. Additionally, the Sutherland constants for CO_2 are listed as S_μ = 222 K and S_k = 1800 K.

Mirels provides a similarity variable, η, for solving the compressible boundary layer equations as shown in Eq. 19.

$$\eta = \sqrt{\frac{1}{2}\frac{u_e \rho_e}{x \mu_e}} \int_0^y \frac{T_e}{T} dy \tag{19}$$

In shock fixed coordinates, the boundary conditions of Mirels are shown in Eq. 20 - 24.

$$u(x, 0) = -U_{is} \tag{20}$$

$$v(x, 0) = 0 \tag{21}$$

$$T(x, 0) = T_w \tag{22}$$

$$u(x, \infty) = u_2 \tag{23}$$

$$T(x, \infty) = T_2 \tag{24}$$

The velocity in the x direction at the wall is determined from the no-slip condition. The y velocity at the wall is zero. The wall temperature is held fixed, and the freestream temperature and velocity determined from the normal shock

relations are enforced at $\eta = \infty$.

There are multiple ways to numerically solve this system of equations using modern methods. For this study, the solution method of Oz et al. [21] for the compressible boundary layer of air over a flat plate was combined with Mirel's theory to estimate the compressible boundary layer properties behind a stationary shock wave in a CO_2 test gas. A 4th order Runge-Kutta method is utilized with a shooting method to close the system of equations and allow a numerical solution. The freestream velocity and temperature ($\eta = \infty$) are used as the convergence criteria. Once the similarity solution is obtained, Eq. 25 is applied to transform the η back to x and y coordinates.

$$y\sqrt{\frac{1}{2}\frac{u_e\rho_e}{x\mu_e}} = \int_0^{\eta} \frac{T}{T_e} d\eta \tag{25}$$

A typical boundary layer temperature profile is presented in Fig. 12. The temperature trends from the wall temperature (~ 297 K) to the core flow temperature (2000 – 3500 K) within the boundary layer thickness (see the δ_{99} curve in Fig. 12). Additionally, the number density is inversely related to the temperature profile, resulting in approximately ten times more CO_2 near the wall than in the freestream (core) flow. This boundary layer code was found to be within 10% of the boundary layer estimated in the LASTA code [22] (when comparing up to 10 cm behind the shock front) which utilizes a slightly different approach in the estimation of the boundary layer though still based on Mirels Theory.

The absorbance signal of the boundary layer can be estimated at the measured locations behind the incident shock wave now that the size (pathlength), temperature, and density of the region is characterized. This simulated boundary layer absorbance is then subtracted from the line of sight (LOS) measurement as shown in 12 and is refit to estimate a new temperature and number density of CO_2. It is seen that the cool boundary layer affects the $\nu_3(00^00)$ R(58) feature significantly more than the $\nu_3(01^10)$ R(103), R(104), and R(140) features. This is highlighted in Fig. 13 which shows the simulated area difference [%] of three spectral features as a function of temperature outside the boundary layer. This is due to the temperature dependent linestrength curve, as low temperature CO_2 does not produce a strong spectral signal in the $\nu_3(01^10)$ R(103), R(104), and R(140) features.

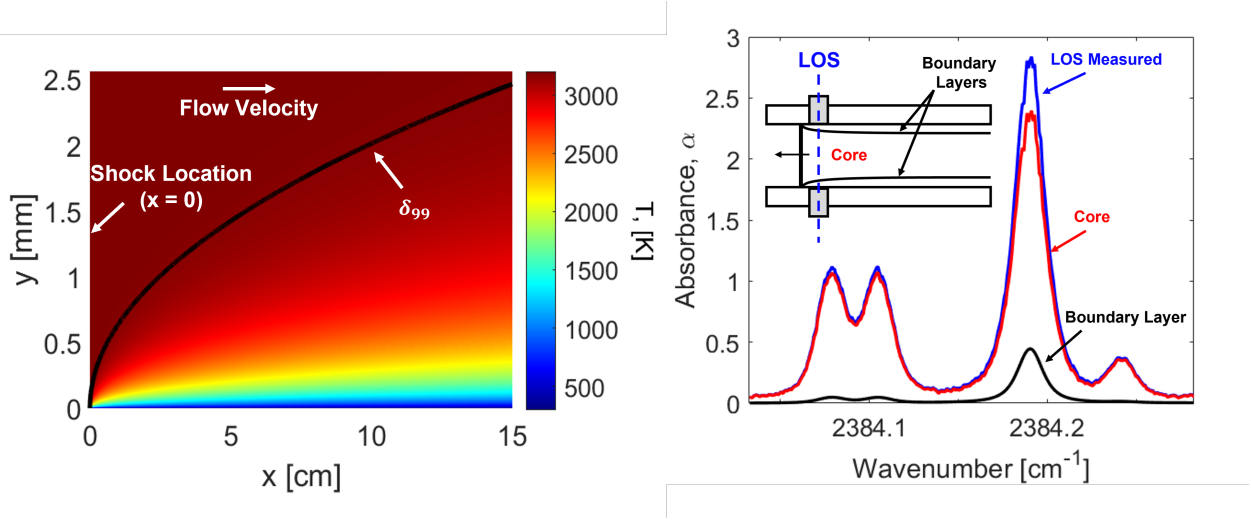

Fig. 12 (left) Simulated compressible boundary layer temperature profile. The shock location, δ_{99} thickness and freestream flow direction are highlighted. The no slip condition is enforced at the wall (y = 0). (right) Absorbance signals from the line of sight (blue), core (red), and boundary layer (black) estimated from a similarity solution of the boundary layer profile.

As can be clearly seen, the temperature of CO_2 increases as well as the CO_2 number density when accounting for the boundary layer in this high temperature case. The low velocity, chemically frozen result is minimally affected by the boundary layer as the $\nu_3(00^00)$ R(58) feature is optically thick and remains above the absorbance cutoff limit in the fit upon subtraction of the simulated boundary layer. In summary, the $\nu_3(00^00)$ R(58) absorbance signal has been shown to be sensitive to a boundary layer affecting ~2% of the 10.16 cm total pathlength. Accounting for a simulated laminar boundary layer increases the LAS CO_2 temperature typically less than 5% and increases the inferred number density by

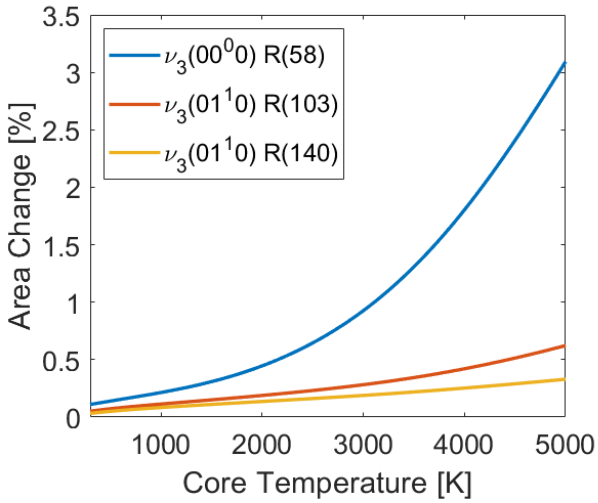

Fig. 13 Line area change due to the boundary layer. The higher energy states are less sensitive to the boundary layer.

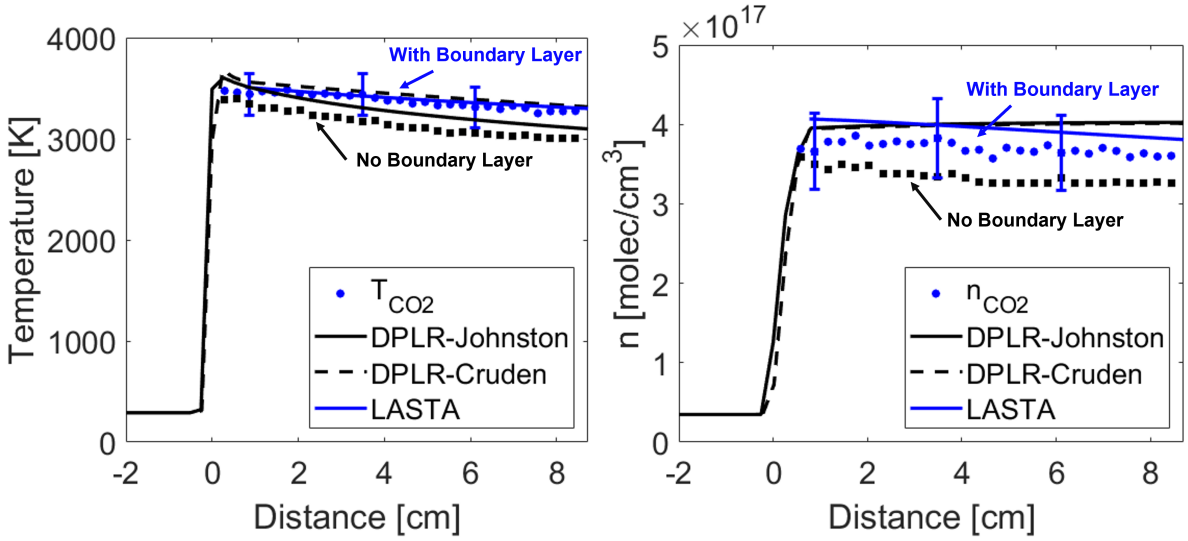

Fig. 14 (left) Temperature and (right) number density vs distance behind shock estimated with LOS absorbance spectrum (black) and estimated with a simulated boundary layer profile (blue). Data is compared with the Cruden [4] and Johnston [5] mechanisms simulated in DPLR [17] and LASTA [22].

approximately 10% (see Fig. 14). Importantly, this explains much of the discrepancy in number density measurement in the reacting regime, and also alters the interpretation of the rate chemistry based upon the temperature trend.

C. Multi-temperature area fitting method

An alternative method to the single temperature spectrum fitting method is explored in this section to minimize the effect of the boundary layer, and high velocity test case results are found to increase to values closer to the DPLR models. The $\nu_3(00^00)$ R(58) absorbance signal is the primary source of boundary layer induced bias in the measurement (see Fig. 13). A rotational temperature of CO_2 can be determined from the spectra via the area ratio between the $\nu_3(01^10)$ R(103) and the $\nu_3(01^10)$ R(140) signals, and as Fig. 13 shows, should be more robust to boundary layer effects. This method was previously utilized by Jelloian et al. [8] to measure CO_2 rotational temperatures in vibrationally relaxing mixtures. The reader is referred to [8] for details on fitting method, sensitivity, and uncertainty analysis using this technique.

The measured rotational temperature can be used on chemically frozen cases to infer vibrational temperature through the conservation of stagnation enthalpy shown in Eq. 26. $h_{0,1}$ and $h_{0,2}$ are the stagnation enthalpy [J/kg] before and after the shock passes.

$$h_{0,1} = h_{0,2} = h_f^o + C_{p,tr-rot}(T_{rot} - T_{ref}) + h_{vib}(T_{vib}) - h_{vib}(T_{ref}) + \frac{u_2^2}{2} \tag{26}$$

h_f^o is the enthalpy of formation [J/kg], $C_{p,tr-rot}$ is the heat capacity at constant pressure [J/(kg·K)], h_{vib} [J/kg] is the enthalpy contribution from the vibrational energy, and u_2 [m/s] is the flow velocity behind the incident shock in the shock fixed frame of reference. Note the flow velocity (u_2) changes during vibrational relaxation by approximately 300 m/s on a majority of the test cases, however this is only attributable to about 3% of the total enthalpy of the flow. Therefore for this analysis, the vibrationally equilibrated flow velocity is used throughout the test. To calculate $C_{p,tr-rot}$ an expression is given in Eq. 27 which assumes the translational and rotational energy mode are equilibrated ($T_{tr} = T_{rot}$) and fully excited.

$$C_{p,tr-rot} = R + \frac{3}{2}R + \frac{D_{rot}}{2}R \tag{27}$$

R is the gas constant, and D_{rot} is the rotational degrees of freedom (for linear molecules such as CO_2, $D_{rot} = 2$). Utilizing Eqs. 26 and 27, the vibrational temperature can be determined on chemically frozen test cases.

Vibrational relaxation was observed on a few low velocity test cases and multi-temperature measurements are presented in Figs. 15 and 16. Figure 15 shows clear trends from near the vibrationally frozen temperature (~ 3000 K) to the vibrationally equilibrated temperature (~ 1880 K). The estimated uncertainty in T_{rot} at this shock velocity is 4.3 %. On many test cases, the vibrational relaxation times measured are slightly longer than the model employed in the DPLR code [17]. As velocities increase and the gas begins to dissociate, the relaxation times decrease to < 1 μs and a single temperature is assumed over all energy modes of CO_2.

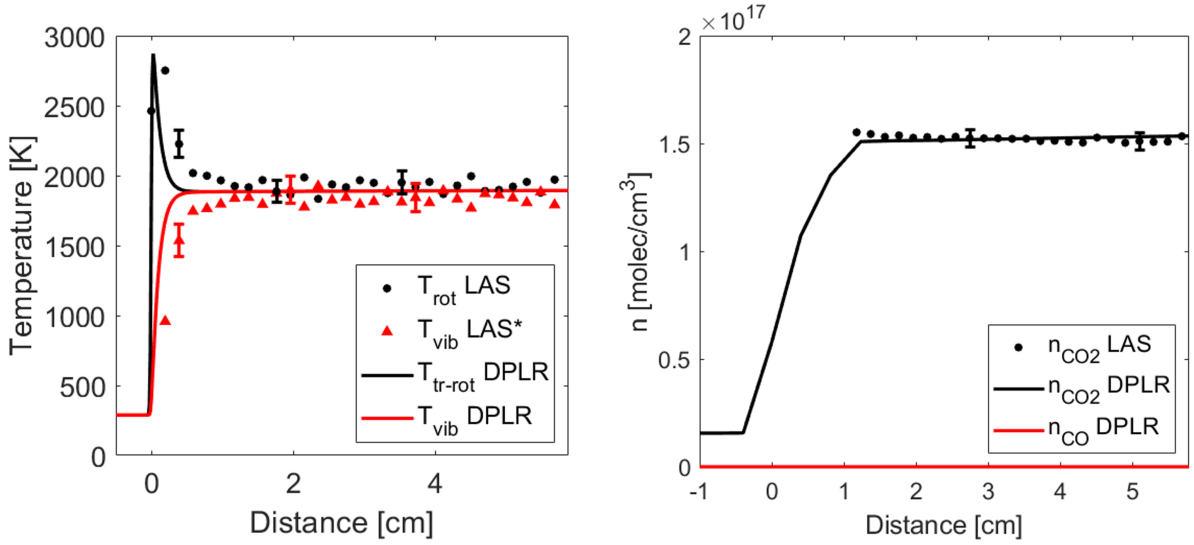

Fig. 15 Time resolved rotational and vibrational temperature (left) and number density (right) for a 1.96 km/s shock with 0.49 Torr fill pressure. The vibrational temperature is determined from conservation of enthalpy assuming $T_{tr} = T_{rot}$.

The differences between measured LAS inferred properties (T and n_{CO_2}) and the DPLR model predictions on chemically reacting test cases have been decreased using the area ratio method with a simulated boundary layer (Figs. 17 - 19). It is observed that the temperature results determined with the area ratio plus boundary layer method have slightly increased the temperature measurement (<5%) and more significantly increased the number density measurement of CO_2 (<10%) with the high velocity cases showing the most significant change. Additionally, in order to measure a rotational temperature, the $\nu_3(01^10)$ R(140) feature must have sufficient signal. On the two lowest velocity test cases (1.30 and 1.39 km/s) , the $\nu_3(01^10)$ R(140) feature was not sufficiently resolved and thus this area ratio method cannot be used. The new fitting method results are summarized in Fig. 19. Overall, good agreement is still found with the

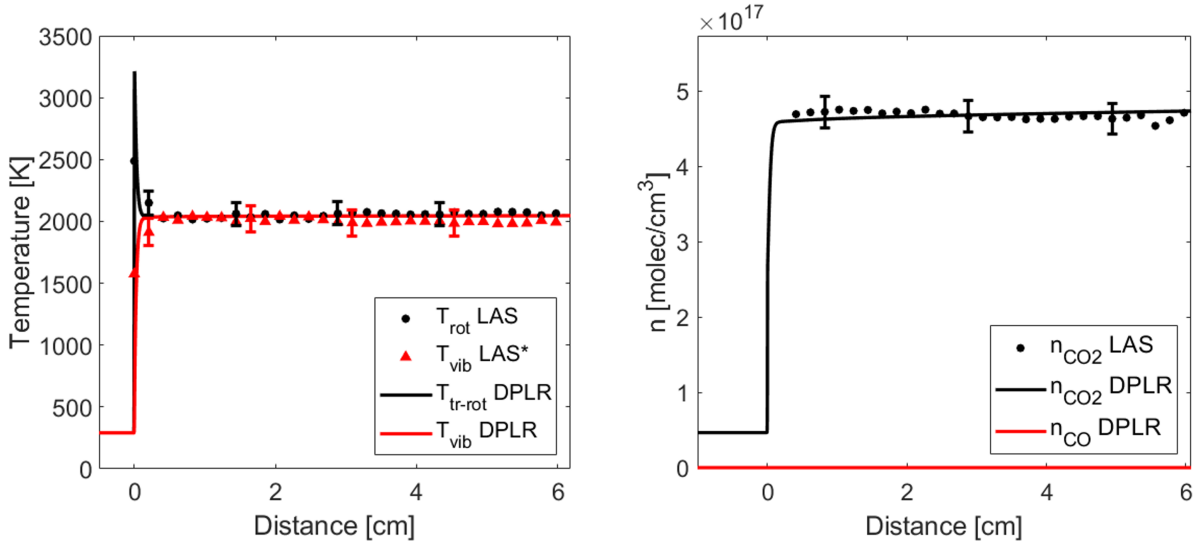

Fig. 16 Time resolved rotational and vibrational temperature (left) and number density (right) for a 2.06 km/s shock with 1.49 Torr fill pressure. The vibrational temperature is determined from conservation of enthalpy assuming $T_{tr} = T_{rot}$.

Johnston [5] mechanism, although a number of tests yield data that lies between the Johnston and Cruden mechanisms at the highest shock velocities. At velocities > 3.1 km/s, the measured number density of CO_2 is lower than any model, however the residuals between model and measurement are decreased relative to Fig. 11.

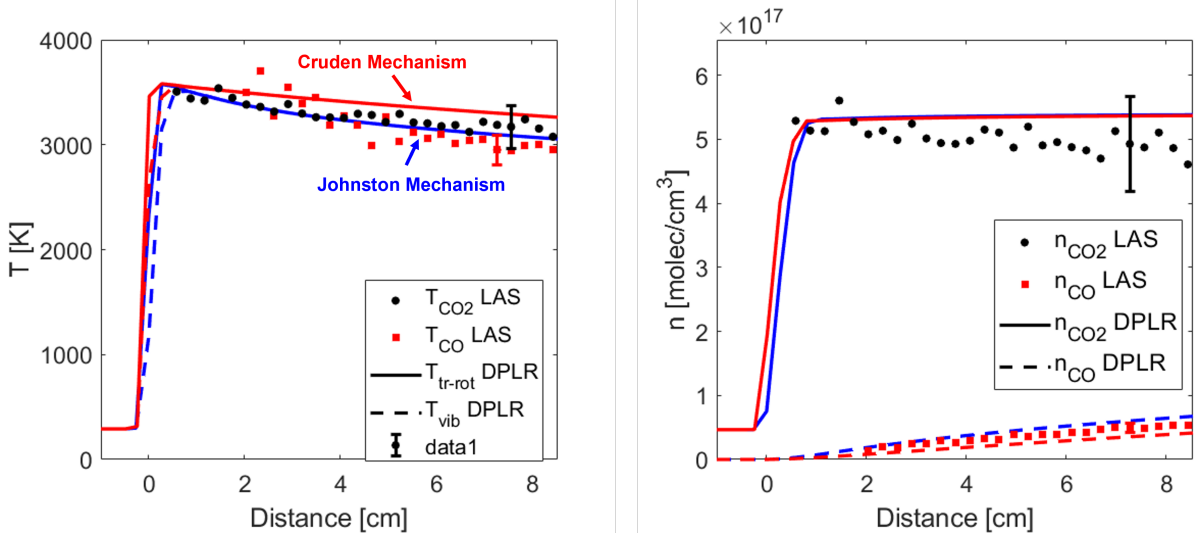

Fig. 17 Spatially resolved rotational temperature (left) and number density (right) for a 2.91 km/s shock with 1.49 Torr fill pressure. Boundary layer correction applied to CO_2.

V. Conclusions

A mid-infrared laser absorption diagnostic has yielded quantitative measurements of temperature and number density of CO_2 and CO at shock conditions relevant to the MEDLI2 heat flux data [1–3] captured during the Mars2020 EDL. Initially, the spectrum was fit with a one temperature model and was found to be sensitive to a thin (1 – 2 mm) boundary layer at shock velocities above 2.7 km/s. The spectra were re-fit using a simulated boundary layer and methods

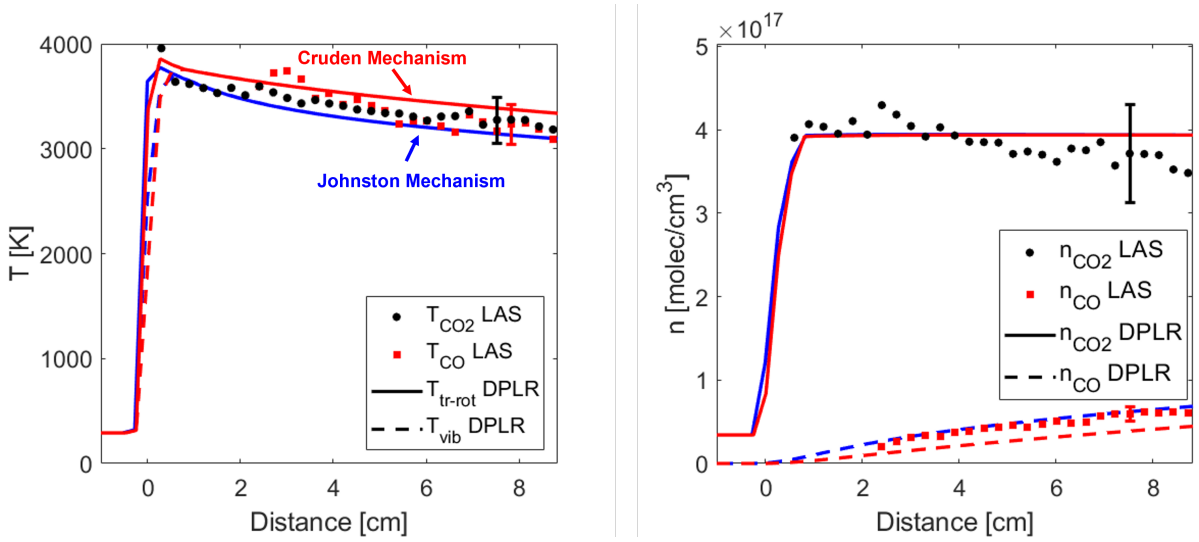

Fig. 18 Spatially resolved rotational temperature (left) and number density (right) for a 3.01 km/s shock with 1.09 Torr fill pressure. Boundary layer correction applied to CO_2.

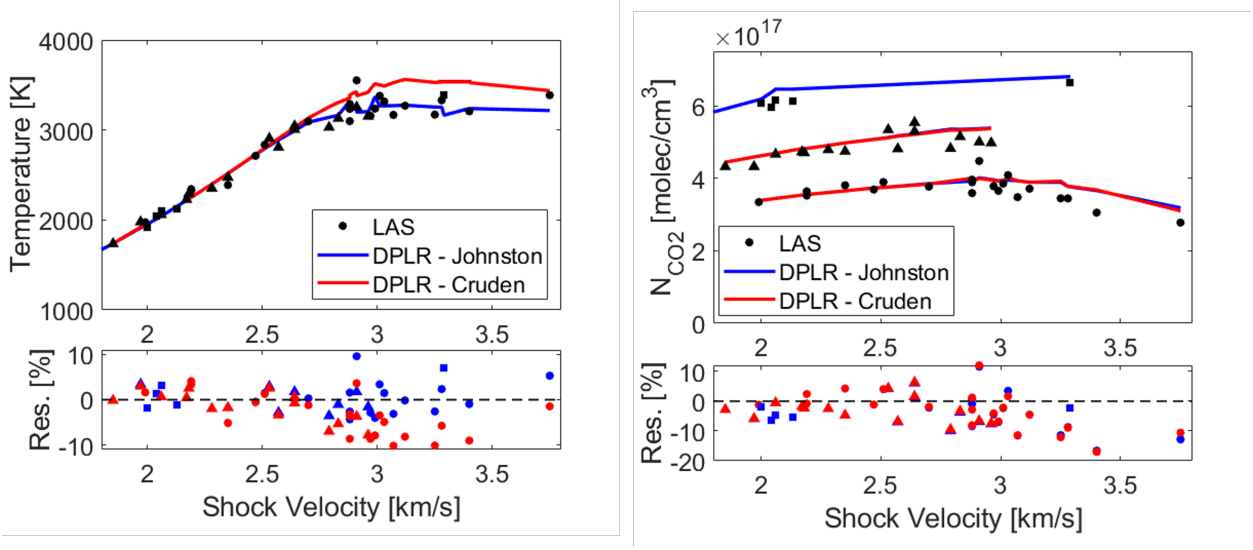

Fig. 19 Measured temperature (left) and CO_2 number density (right) vs shock velocity. Data is compared with the Cruden [4] and Johnston [5] mechanisms simulated in DPLR [17]. Squares, triangles, and circles denote a fill pressure of 1.99, 1.49, and 1.09 Torr respectively.

that isolate the energy modes as developed in [8]. The resulting temperature and number density plots were found to be more robust to the boundary layer effect (up to velocities ~3.1 km/s) and yield results closer to the DPLR models (typically within 5% for temperature and 10% for number density).

Independent spectral fitting over CO_2 and CO has yielded similar temperature results typically within 5% of the estimated temperature from simulation. A slight decrease is observed on the number density of CO_2 that is not captured in the DPLR model. This is likely due to an adverse pressure gradient in the simulation while the shock tube has a decreasing pressure gradient behind the shock wave. Multi-temperature measurements were made at low velocities and relaxation times were found to be slightly longer than those predicted by the DPLR model [17].

In summary, the LAS sensor and method described above have been used in tandem with optical emission spectroscopy (OES) to measure a recreated Mars entry shock layer to further the investigation of the MEDLI2 flight data and increase the science return of the Mars2020 mission. The emission data is the subject of a companion paper [9],

however, the resulting trends in inferred temperature and number density from OES and LAS largely agree within their respective uncertainties. Further experimental studies of the boundary layer size are warranted to assess the accuracy of the simulations and assumptions utilized in this work, though these simulations have shown good agreement with an independent code (LASTA [22]) and successfully explain a gap between the LAS measurements and models on reacting test cases. CO_2 non-equilibrium kinetics are complex, and the data produced in this work and [9] can be used to refine and tune the rate models utilized in this environment.

Acknowledgments

The authors acknowledge Ramon Martinez and the EAST Facilities staff for their support and technical expertise. The authors acknowledge Anil P. Nair and Kevin K. Schwarm for their expertise in fiber alignment and portable sensor design. Nicolas Q. Minesi acknowledges support from NASA's Space Technology Research Grants Program (award no. 80NSSC21K0066). Christopher C. Jelloian is supported by a NASA Space Technology Research Fellowship (award no. 80NSSC18K1158).

References

[1] Cruden, B. A., Miller, R. A., Brandis, A. M., Tibere-Inglesse, A. C., Jelloian, C. C., Spearrin, R. M., West, T. K., Johnston, C. O., Prabhu, D. K., Monk, J., Clarke, J., Mare, L. D., and McGilvray, M., "MARS 2020 BACKSHELL RADIATIVE HEATING MEASUREMENT AND SHOCK TUBE VERIFICATION," *9th International Workshop on Radiation of High Temperature Gases for Space Missions*, Santa Maria, Azores, Portugal, 2022.

[2] Miller, R. A., Tang, C. Y., White, T. R., and Cruden, B. A., "MEDLI2: MISP Measured Aftbody Aerothermal Environments," *AIAA Science and Technology Forum and Exposition, AIAA SciTech Forum 2022*, American Institute of Aeronautics and Astronautics Inc, AIAA, 2022. https://doi.org/10.2514/6.2022-0551.

[3] Tang, C. Y., Mahzari, M., Prabhu, D. K., Alpert, H. S., and Cruden, B. A., "MEDLI2: MISP Inferred Aerothermal Environment and Flow Transition Assessment," *AIAA Science and Technology Forum and Exposition, AIAA SciTech Forum 2022*, American Institute of Aeronautics and Astronautics Inc, AIAA, 2022. https://doi.org/10.2514/6.2022-0552.

[4] Cruden, B. A., Prabhu, D. K., and Brandis, A. M., "Measurement and characterization of mid-wave infrared radiation in CO2 shocks," *AIAA AVIATION 2014 -11th AIAA/ASME Joint Thermophysics and Heat Transfer Conference*, American Institute of Aeronautics and Astronautics Inc., 2014. https://doi.org/10.2514/6.2014-2962.

[5] Johnston, C., and Brandis, A., "Modeling of nonequilibrium CO Fourth-Positive and CN Violet emission in CO 2 –N 2 gases," *Journal of Quantitative Spectroscopy and Radiative Transfer*, Vol. 149, 2014, pp. 303–317. https://doi.org/10.1016/j.jqsrt.2014.08.025, URL http://dx.doi.org/10.1016/j.jqsrt.2014.08.025https://linkinghub.elsevier.com/retrieve/pii/S0022407314003690.

[6] White, T. R., Mahzari, M., Miller, R. A., Tang, C. Y., Monk, J., Santos, J. A., Karlgaard, C. D., Alpert, H. S., Wright, H. S., and Kuhl, C., "Mars entry instrumentation flight data and mars 2020 entry environments," *AIAA Science and Technology Forum and Exposition, AIAA SciTech Forum 2022*, American Institute of Aeronautics and Astronautics Inc, AIAA, 2022. https://doi.org/10.2514/6.2022-0011.

[7] Jelloian, C. C., Bendana, F. A., Wei, C., Spearrin, R. M., and Macdonald, M. E., "Nonequilibrium Vibrational, Rotational, and Translational Thermometry via Megahertz Laser Absorption of CO," *Journal of Thermophysics and Heat Transfer*, Vol. 36, No. 2, 2022, pp. 266–275. https://doi.org/10.2514/1.T6376.

[8] Jelloian, C. C., Minesi, N. Q., and Spearrin, R. M., "High-speed mid-infrared laser absorption spectroscopy of CO$$_2$$ for shock-induced thermal non-equilibrium studies of planetary entry," *Applied Physics B*, Vol. 128, No. 12, 2022, p. 216. https://doi.org/10.1007/s00340-022-07934-4, URL https://link.springer.com/10.1007/s00340-022-07934-4.

[9] Tibère-Inglesse, A. C., Cruden, B. A., Jelloian, C. C., and Spearrin, R. M., "Examination of Mars2020 shock-layer conditions via infrared emission spectroscopy of CO2," *AIAA SciTech Conference*, 2023.

[10] Hanson, R., Spearrin, R., and Goldenstein, C., *Spectroscopy and Optical Diagnostics for Gases*, Springer International Publishing, 2016. https://doi.org/10.1007/978-3-319-23252-2.

[11] Rothman, L., Gordon, I., Barber, R., Dothe, H., Gamache, R., Goldman, A., Perevalov, V., Tashkun, S., and Tennyson, J., "HITEMP, the High-Temperature Molecular Spectroscopic Database," *Journal of Quantitative Spectroscopy and Radiative Transfer*, Vol. 111, No. 15, 2010, pp. 2139–2150. https://doi.org/10.1016/j.jqsrt.2010.05.001.

[12] Palmer, G., and Cruden, B. A., "Experimental validation of CO2 radiation simulations," *43rd AIAA Thermophysics Conference 2012*, 2012. https://doi.org/10.2514/6.2012-3188.

[13] Cruden, B. A., Martinez, R., Grinstead, J. H., and Olejniczak, J., "Simultaneous vacuum ultraviolet through near IR absolute radiation measurement with spatiotemporal resolution in an Electric Arc Shock Tube," *41st AIAA Thermophysics Conference*, American Institute of Aeronautics and Astronautics Inc., 2009. https://doi.org/10.2514/6.2009-4240.

[14] Trainer, M. G., Wong, M. H., McConnochie, T. H., Franz, H. B., Atreya, S. K., Conrad, P. G., Lefèvre, F., Mahaffy, P. R., Malespin, C. A., Manning, H. L., Martín-Torres, J., Martínez, G. M., McKay, C. P., Navarro-González, R., Vicente-Retortillo, , Webster, C. R., and Zorzano, M. P., "Seasonal Variations in Atmospheric Composition as Measured in Gale Crater, Mars," *Journal of Geophysical Research: Planets*, Vol. 124, No. 11, 2019, pp. 3000–3024. https://doi.org/10.1029/2019JE006175.

[15] Park, C., Howe, J. T., Jaffe, R. L., and Candler, G. V., "Review of chemical-kinetic problems of future NASA missions, II: Mars entries," *Journal of Thermophysics and Heat Transfer*, Vol. 8, No. 1, 1994, pp. 9–23. https://doi.org/10.2514/3.496.

[16] Simpson, C. J. S. M., and Chandler, T. R. D., "A shock tube study of vibrational relaxation in pure CO2 and mixtures of CO2 with the inert gases, nitrogen, deuterium and hydrogen," Tech. rep., 1970.

[17] Wright, M. J., White, T., and Mangini, N., "Data Parallel Line Relaxation (DPLR) Code User Manual Acadia-Version 4.01.1," Tech. rep., 2009. URL https://ntrs.nasa.gov/search.jsp?R=20110006930.

[18] Cruden, B. A., Brandis, A. M., and Macdonald, M. E., "Characterization of CO thermochemistry in incident shockwaves," *2018 Joint Thermophysics and Heat Transfer Conference*, 2018, pp. 1–22. https://doi.org/10.2514/6.2018-3768.

[19] MIRELS, H., "Boundary Layer Behind Shock or Thin Expansion Wave Moving Into Stationary Fluid," *NACA Tech. Note 3712*, 1956.

[20] White, F. M., *Viscous Fluid Flow*, 3rd ed., McGraw-Hill, New York, NY, 2006.

[21] Oz, F., and Kara, K., "A CFD Tutorial in Julia: Introduction to Compressible Laminar Boundary-Layer Flows," *Fluids*, Vol. 6, No. 400, 2021.

[22] Satchell, M., McGilvray, M., and Di Mare, L., "Analytical Method of Evaluating Nonuniformities in Shock Tube Flows: Theory and Development," *AIAA Journal*, Vol. 60, No. 2, 2022, pp. 654–668. https://doi.org/10.2514/1.J060990.